CM² MAGAZINE

第 16 期

南方科技大学海洋磁学中心主编

创刊词

海洋是生命的摇篮，是文明的纽带。地球上最早的生命诞生于海洋，海洋里的生命最终进化成了人类，人类的文化融合又通过海洋得以实现。人因海而兴。

人类对海洋的探索从未停止。从远古时代美丽的神话传说，到麦哲伦的全球航行，再到现代对大洋的科学钻探计划，海洋逐渐从人类敬畏崇拜幻想的精神寄托演变成可以开发利用与科学研究的客观存在。其中，上个世纪与太空探索同步发展的大洋科学钻探计划将人类对海洋的认知推向了崭新的纬度：深海（deep sea）与深时（deep time）。大洋钻探计划让人类知道，奔流不息的大海之下，埋藏的却是亿万年的地球历史。它们记录了地球板块的运动，从而使板块构造学说得到证实；它们记录了地球环境的演变，从而让古海洋学方兴未艾。

在探索海洋的悠久历史中，从大航海时代的导航，到大洋钻探计划中不可或缺的磁性地层学，磁学发挥了不可替代的作用。这不是偶然，因为从微观到宏观，磁性是最基本的物理属性之一，可以说，万物皆有磁性。基于课题组的学科背景和对海洋的理解，我们对海洋的探索以磁学为主要手段，海洋磁学中心因此而生。

海洋磁学中心，简称 CM^2，一为其全名“Centre for Marine Magnetism”的缩写，另者恰与爱因斯坦著名的质能方程 $E = MC^2$ 对称，借以表达我们对科学巨匠的敬仰和对科学的不懈追求。

然而科学从来不是单打独斗的产物。我们以磁学为研究海洋的主攻利器，但绝不仅限于磁学。凡与磁学相关的领域均是我们关注的重点。为了跟踪反映国内外地球科学特别是与磁学有关的地球科学领域的最新研究进展，海洋磁学中心特地主办 CM^2 Magazine，以期与各位地球科学工作者相互交流学习、合作共进！

“海洋孕育了生命，联通了世界，促进了发展”。 21 世纪是海洋科学的时代，由陆向海，让我们携手迈进中国海洋科学的黄金时代

目 录

对科研的理解

刘伟

对科研的理解，在我看来是个很大的命题。似乎要回归到哲学的本质，即“我是谁，我从哪里来，我到哪里去”。

在我有限的认知里，科研是一项社会活动，其主要是满足人类的好奇心，并推动社会的发展。科研来源于西方社会，从最开始的一项贵族活动，逐渐变成了一些人的职业。而关于科研将走向何方，我揣测无论什么时候，它依然是遵循“发现问题-提出假设-验证假设-归纳总结”的模式，只是发现的问题不同，验证假设的手段不同了。当然，谈论这些哲学般的问题都太深奥了，我更想谈谈我为什么选择做科研，我觉得应该如何做科研。

在我的读书生涯里，一直对数学比较感兴趣，喜欢理科，是个标准的理工男。上大学填志愿，只要是理工类的专业就可以。对赚钱的金融经济类专业并不怎么感冒，并愚昧地认为那只是高中数学题里本金、利息和收益之类的简单的无趣的数学计算。而我更享受那种解出一道难题的成就感，并钟爱那种证明题。自己去想方设法的一步步逼近最后的答案。现在想想，这似乎和做科研还是有点像的，就是一步步逼近你想要解决的问题，逼近真相。最后误打误撞的选择了地球科学类专业。坦诚地说，刚开始还是挺失望的，觉得本科学的东西，文科味道太浓厚了，直到上了研究生才慢慢找到当初的感觉。虽然读硕士期间找到了一点点感觉，但是当时油价过低（我是石油地质出身），面对身边各种转行的同学，我自己也想过要不要去转行，或者从政去追求自己的家国情怀（也许一辈子是个默默无闻的基层公务员），或者从商去满足自己对物质的渴望（也许一生只是个跑腿的穷光蛋）。最后思来想去，学术对自己而言应该是最不错的选择。一是自己对科研还是有一点兴趣，想在自己走过一生回首往事时发现自己还是留下了一点东西；二是科研最公平，对我们这些平民百姓应该说最友好；三是赶上了中国发展科研的最好时机，当然竞争也是相当激烈。基于以上三个原因，我就选择了读博士，而最后成为刘老师的学生那又是一段缘分与佳话了。

至于如何做科研，还是我上文提到的，无论如何发展，它依然离不开“发现问题-提出假设-验证假设-归纳总结”的模式。只是这个第一步“发现问题”可能是你导师发现后让你做的，也可能是你自己发现的。发现问题并不难，这个世界有太多未解之谜。提出假设也不难，难得是如何提出合理的假设，这就需要建立在自己对问题的敏锐观察和对前人研究的深入理解的基础上来提出合理假设。只有如此，你的假设才能更可能逼近真相，科研成果也事半功倍。对我们大多数人而言，最难的应该是“验证假设”这一步了。如何验证，在知识储备上，这可能需要你去学习其他学科的内容，多学科交叉；在技术支持上，你可能需要去学习掌握最先进的以前未接触过的技术。当然，这都是方法论的东西，扪心自问，最难的还是坚持，是一如既往的去推进科研进程的能力。这一过程中，你可能突然间动力不足了，或者诱惑太多了，或者情感出问题了，总之你被打断了。然后你会间歇性停顿，也许是一周，也许是一月，还可能是一年。想通了，调整好了，又可以来一段时间的高效率科研了。这就是我目前的状态，应该也是大多数科研人员的状态。最难的不是你不够聪明，是你很难去专注解决这个问题。因为现在你要解决的问题，不再是高中时那种解证明题的问题了，是全新的大家都不知道的问题，所以你必须花更多的时间，保持更充沛的精力，持之以恒，才有可能做出成果。“发现问题-提出假设-验证假设”这一流程下来，我们应该是合格的科研工作者了。而到了科学家这一层次，他应该还会在验证假设的基础上进行归纳总结，在不同的问题中找出共性，总结出普适的理论。

就我个人而言，进行科研时，我觉得逻辑特别重要，我提出的每一个假设，我做的每一件和科研有关的事，都应该是我科研逻辑线上的一个节点。每做一个实验前，我应该对实验有几种预期，我才敢放手去做。即使我觉得某个实验肯定有用，但不在我的逻辑线上，或者由于知识储备暂时没想到连接点，我还是不太喜欢漫无目的的去做实验。这也造成了我有时候畏手畏脚，科研推进的比较慢。

最后，非得总结下自己的科研的理解，那就是“毅力+逻辑”。这两点我都还需要努力！

第 6 章　磁化率概念进二阶

以上对磁化率的定义对应的是直流场的测量。除了直流场，还有交流场测量方式，这种情况要复杂得多。

此时，M 和 H 之间不再同相位，因此就出现了实磁化率(χ′)和虚磁化率(χ″)，对于超顺磁 SP 颗粒，

$$\chi' = \frac{\chi_0}{1+\omega^2\tau^2}$$

$$\chi'' = \omega\tau\frac{\chi_0}{1+\omega^2\tau^2}$$

其中，χ_0 是直流场下的磁化率，$\chi_0 = \frac{\mu_0 V M_s^2}{3kT}$；ω是观测频率；τ是驰豫时间。

可见，SP 颗粒的磁化率受到观测频率的影响。因此，如果样品中含有一定量的 SP 颗粒，如果所用仪器的观测频率不同，其值就无法横向对比。所以我们一定要看清楚研究者所用仪器的型号和所用的观测频率。最新的一款 MFK 磁化率仪器，有三个观测频率。

磁化率和观测频率密切相关，我们可以通过两种方式来探讨这种关系。

第一种最简单，通过上述公式我们立刻就得知磁化率随着频率的增加而减小。

第二种方式则从其物理本质上去理解。对于这些 VSP 颗粒，只要稍微一变动频率它们就可能变换状态。当频率增加时，有一部分 VSP 颗粒就会从 SP 状态变为 SD 状态，其磁化率当然会降低。当频率继续增加的时候，更小的 SP 颗粒会变为 SD 状态，磁化率也会随之继续降低。

我们必须注意到，改变频率，它只对那些处于 SP/SD 边界的 VSP 颗粒产生影响。增加频率，并不影响已经是 SD 状态的颗粒。对于更小的纯 SP 颗粒，也不会产生影响。

重要的事情再说一遍，改变频率，只会对很小的一个粒径范围（处于 VSP

状态）的颗粒产生影响。增加频率，会降低样品的整体磁化率。

早期的 Bartington 磁化率仪器设置了两个频率，低频（Low frequency, LH = 470 Hz）和高频（High frequency, HF = 4700Hz）。所以后来当考虑磁化率频率特性时，频率变化大都遵循一个数量级，比如 1 Hz 和 10 Hz 等等。

现在我们来做一点小变化，我们定义绝对频率磁化率为：

$\chi_{fd} = \chi_{LF} - \chi_{HF}$

这么做的好处在哪里呢？

我们刚才讨论过变化频率只对 VSP 颗粒有影响，对纯 SP 和 SD 颗粒没有影响。低频磁化率和高频磁化率这样一相减，我们就完全消除了纯 SP 和 SD 颗粒的影响，在 VSP 粒径区间，我们得到一个小峰值。

如果χ_{fd}不为零，从严格意义上讲，它只代表着样品含有 VSP 颗粒，而不能百分百确定样品中磁性颗粒的粗细。

但是，自然界不会这么巧合，刚好只含有 VSP 颗粒，这需要非常特殊的地质过程才能形成，概率极低。正常情况，纳米颗粒的粒径都会遵循一定的分布，比如对数正态分布等。就如同我们观察一头大象，不需要看全身，只要看到大象耳朵就知道这是一头大象，并能猜出它身体形状。

所以，当我们检测到 VSP（一般为 20-22 nm）颗粒时，我们就可以推断出，样品中一定还含有更细小的 SP 和更大一点的 SD 颗粒。如果粒径分布比较固定，那么χ_{fd}的绝对值变化就代表着纳米颗粒含量的变化。这对于研究成土过程、风化过程、氧化还原中的矿物转化过程等非常有用。

当χ_{fd}为零时，难道代表着样品中不含有 SP 颗粒？

答案是“否！”

χ_{fd}为零可能对应着两种情况：不存在 VSP 颗粒，或者存在着非常细小的 SP 颗粒。这种情况需要额外的低温实验来加以甄别。因为对于更小的 SP 颗粒，只有在更低温度下才能显示其 SP/SD 转化行为，从而被我们观测到。

除了频率磁化率绝对值，我们还经常定义相对值：

$\chi_{fd}\% = (\chi_{LF} - \chi_{HF})/\chi_{LF} * 100\%$

在这个公式中，把χ_{fd}用低频磁化率进行归一化。

χ_{LF}是一个混合信息，它由样品中所有能产生磁化率的物质共同决定，包括

反铁磁性颗粒、亚铁磁性颗粒，以及顺磁性颗粒等等，这就引入新的复杂性。

我们假设χ_{fd}不变，而样品的χ_{LF}在变，那么χ_{fd}%就会随着χ_{LF}的变化而变化，与χ_{fd}一点关系都没有。

对于χ_{fd}%，其值的变化基本反映颗粒粒径的分布。当处于 SP/SD 临界点附近的颗粒的含量固定时，也就是χ_{fd}固定，此时，随着其粒径分布的加大，更多细小 SP 和大于 SP 的颗粒会贡献分母χ_{LF}，从而χ_{fd}%减小。

但是我们在读之前很多有关中国黄土-古土壤研究的文章时，很多学者把χ_{fd}%和χ_{fd}都定义为夏季风强弱的指标。夏季风高，雨水充沛，成土作用强，产生更多 SP 颗粒，所以χ_{fd}和χ_{fd}%都会增加。这种现象确实被观测到了，难道和上面的解释有冲突？

造成χ_{fd}%被误解释的原因如下：

对于古土壤，χ_{LF}主要由两部分组成：

$\chi_{LF} = \chi_{物源} + \chi_{成土}$，

其中$\chi_{成土}$与χ_{fd}成正比，也就是$\chi_{成土} = A*\chi_{fd}$，A 是一个常量。

如果我们把$\chi_{物源}$给扣除掉，我们立即就会发现，$\chi_{fd}\% = 1/A$，这是一个常量，与成土作用的强弱并没有关系。

所以，很多不正确的参数用法刚好凑巧能解释自然现象。

除了磁化率外，频率磁化率也是温度的函数。在 300 K，对应 1 Hz 和 10 Hz 的 VSP 窗口在 25 nm 左右。而在 50 K，频率磁化率反映的是 13 nm 的颗粒。

这很好理解。当温度降低时，那些大一点的纳米颗粒就变成了 SD 颗粒，对χ_{fd}没有贡献，所以 VSP 的窗口就会向更小粒径范围移动。

在不同温度下(曲线上方的数值，单位为 K)，频率磁化率所对应的反映 SP/SD 临界窗口。随着观测温度增加，频率磁化率反映的 SP 颗粒粒径越大($D_{\chi fd\text{-}max}$)。因此，可以构建$D_{\chi fd\text{-}max}$与观测温度的相关曲线。也就是说，根据图 4 的转换曲线可以获得 SP 颗粒的粒径分布信息。

该方法已经在中国黄土-古土壤序列中得到很好的应用。图 5 显示了古土壤中典型样品的$\chi_{fd}-T$ 曲线，以及通过$\chi_{fd}-T$ 曲线和$D_{\chi fd\text{-}max}$-T 曲线得到的古土壤中成土作用产生的纳米磁赤铁矿的粒径分布。可见，SP 磁赤铁矿的粒径分布与其成土强度关系不大。因此，古土壤的磁性增强主要由 SP 磁赤铁矿含量增加引起。

文献导读

1. 间冰期 MIS-13 期异常强烈的东亚夏季风可能与拉尼拉模态有关

翻译人：仲义 zhongy@sustech.edu.cn

H. Lu, Q.Z. Yin, J. Jia et al., ***Possible link of an exceptionally strong East Asian summer monsoon to a La Nina-like condition during the interglacial MIS-13*** *[J]. Quaternary Science Reviews, 2020, 227. 106048.*

摘要：中国黄土高原东部和中部的研究显示 S5-1 古土壤层对应于海洋氧同位素（MIS）13 期是过去几百年间变化最强烈，说明该时期东亚夏季风（EASM）最强。然而，证据显示在 S5-1 古土壤形成的相对强度存在区域多样性。本文中我们首次整合所有黄土高原地区的 S5-1 土壤层变化曲线，并利用不同黄土-古土壤剖面的磁化率空间变化来识别出在 MIS-13 时期的东亚夏季风强度变化。我们同样比较中国其他区域的季风黄土记录，结果显示，在黄土高原中部地区，S5-1 层确实如前人研究一样出现最强，而在黄土高原西部区域，S5-1 层出现减弱，而 S4 古土壤层在 MIS11 时期出现最强。相比于 MIS-11 时期，MIS 13 时期的东亚夏季风的北部锋面无法到达黄土高原西部，但是锋面位置更偏北和东方向。基于热带太平洋海表温度数据，我们认为这种 MIS-13 期出现时间和空间上异常特征可能与强烈的 La Nina 气候模态有关。在种气候环境下，西太平洋副热带高压（WPSH）减弱，并向东北方向后退，导致中国中东部的降水增加而西部内陆的降水减少。

ABSTRACT: Previous studies from the central and eastern Chinese Loess Plateau (CLP) showed that the S5-1 paleosol, which corresponding to Marine Isotope Stage (MIS) 13, was the strongest developed during the last million years, suggesting extremely strong East Asian summer monsoon (EASM). However, evidence shows that regional diversity exists in the relative intensity of the S5-1 soil formation. In this study, we first verify systematically the S5-1 soil development across the whole CLP by using numerous loess records. We then examine the spatial variation of the magnetic susceptibility of different loess-paleosol sections to identify the spatial change of the EASM intensity during MIS-13. We also compare the loess records with other monsoon records in China. Our results show that, in central CLP, S5-1 is indeed the strongest developed as suggested by

previous studies, whereas in the western CLP, it is weakly developed and the S4 paleosol developed during MIS-11 is the strongest. As compared to MIS-11, the northern front of the EASM during MIS-13 didn't penetrate into western CLP, but was located more northerly and eastward. Based on sea surface temperature records in the tropical Pacific, we suggest that the temporal and spatial abnormal variation of the EASM during MIS-13 could be related to a strong La Nina or La ~ Nina-like climate condition. Under such condition, the Western Pacific Subtropical High (WPSH) becomes weaker and retreats more northeastward, leading to more precipitation in the mid-east region of northern China but less rainfall in the western inland.

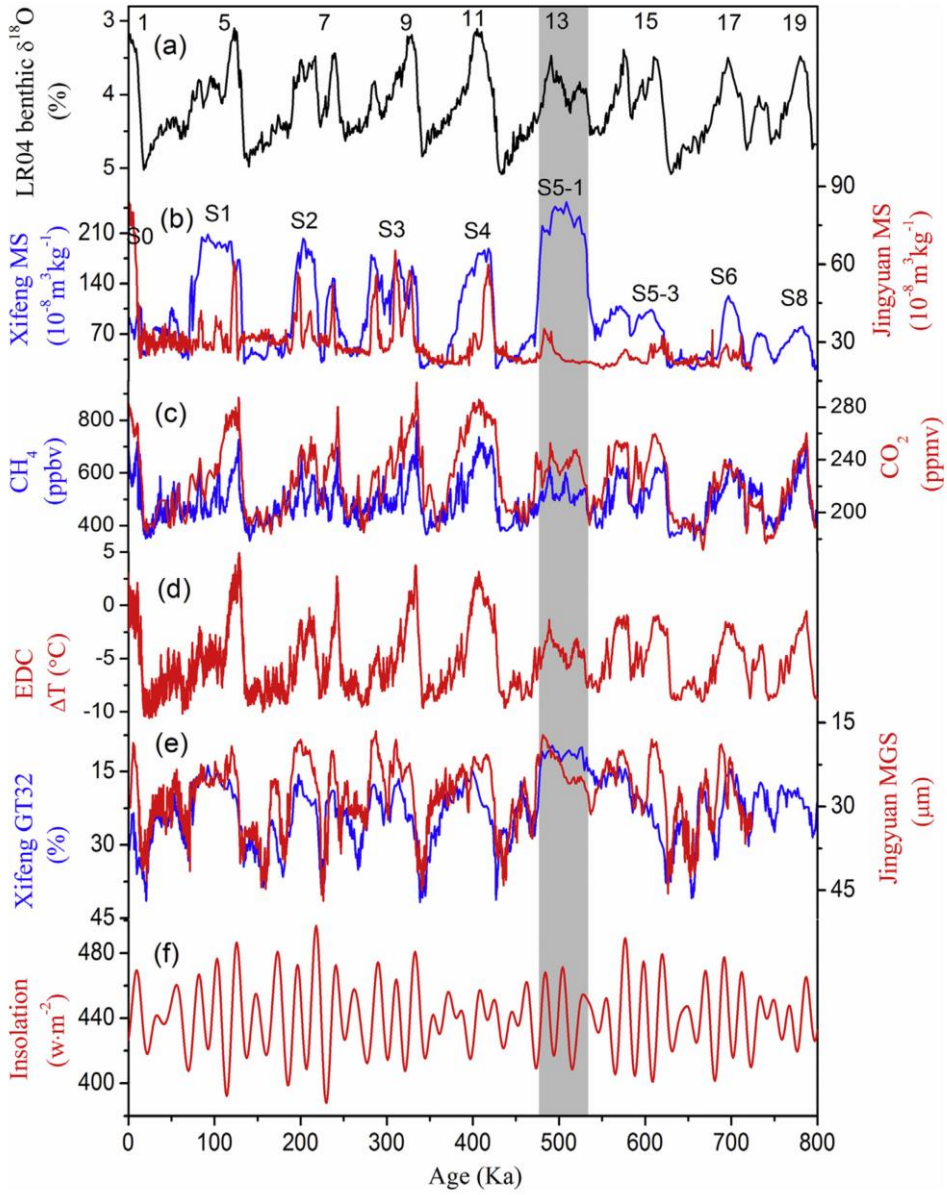

Figure 1. Comparison of the China loess proxies of East Asian monsoon with relevant ice, marine records and insolation. (a) Marine d18O record (black) (Lisiecki and Raymo, 2005) with the interglacials oxygen isotope stages

(MIS) labelled at the top part; (b) loess magnetic susceptibility at Xifeng (blue) (Guo et al., 2009) and Jingyuan (red) (Sun et al., 2006a) with the major paleosol units labelled; (c) Antarctic CH4 (blue) (Loulergue et al., 2008) and CO2 records (red) (Lüthi et al., 2008); (d) EDC DT record (red) (Jouzel et al., 2007); (e) loess grain size GT32 (>32 mm %) and MGS (mean grain size) at Xifeng (blue) (Guo et al., 2009), Jingyuan (red) (Sun et al., 2006a); (f) July insolation 65N (Berger and Loutre, 1991). Gray frame denote the proxies for which MIS-13 can be considered as typical from an amplitude signal point of view. (For interpretation of the references to color in this figure legend, the reader is referred to the Web version of this article.)

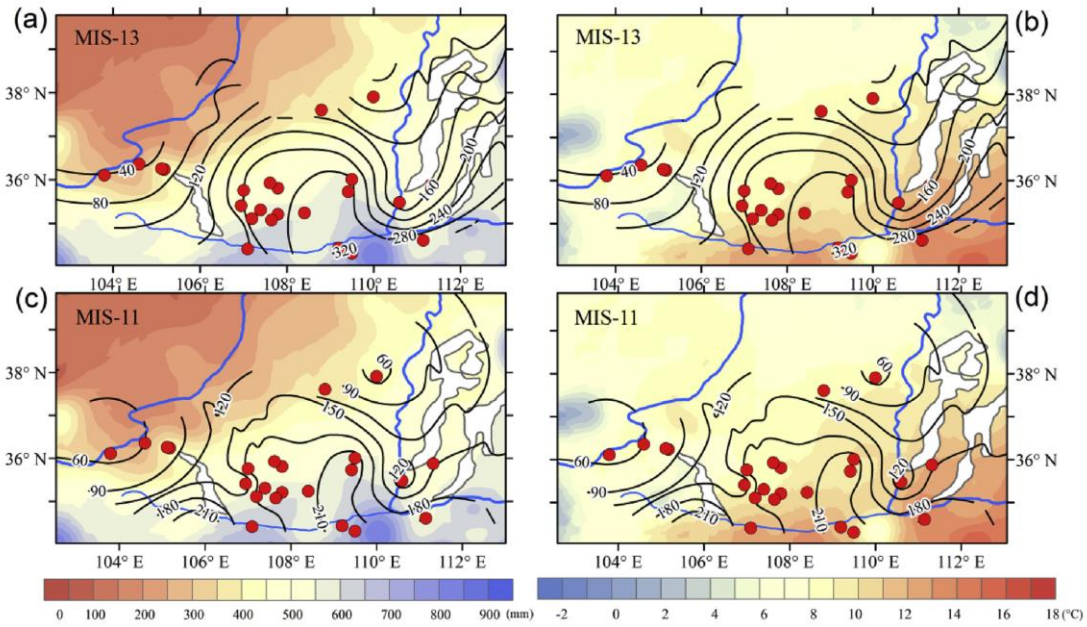

Figure 2. Magnetic susceptibility (108 $m^3 kg^1$) contour maps for the MIS-13 (a and b) and MIS-11 (c and d), together with modern mean annual precipitation (a and c) and temperature (b and d) over 51 y (1951e2001). The contour maps were constructed using magnetic susceptibility data from 25 loess sections.

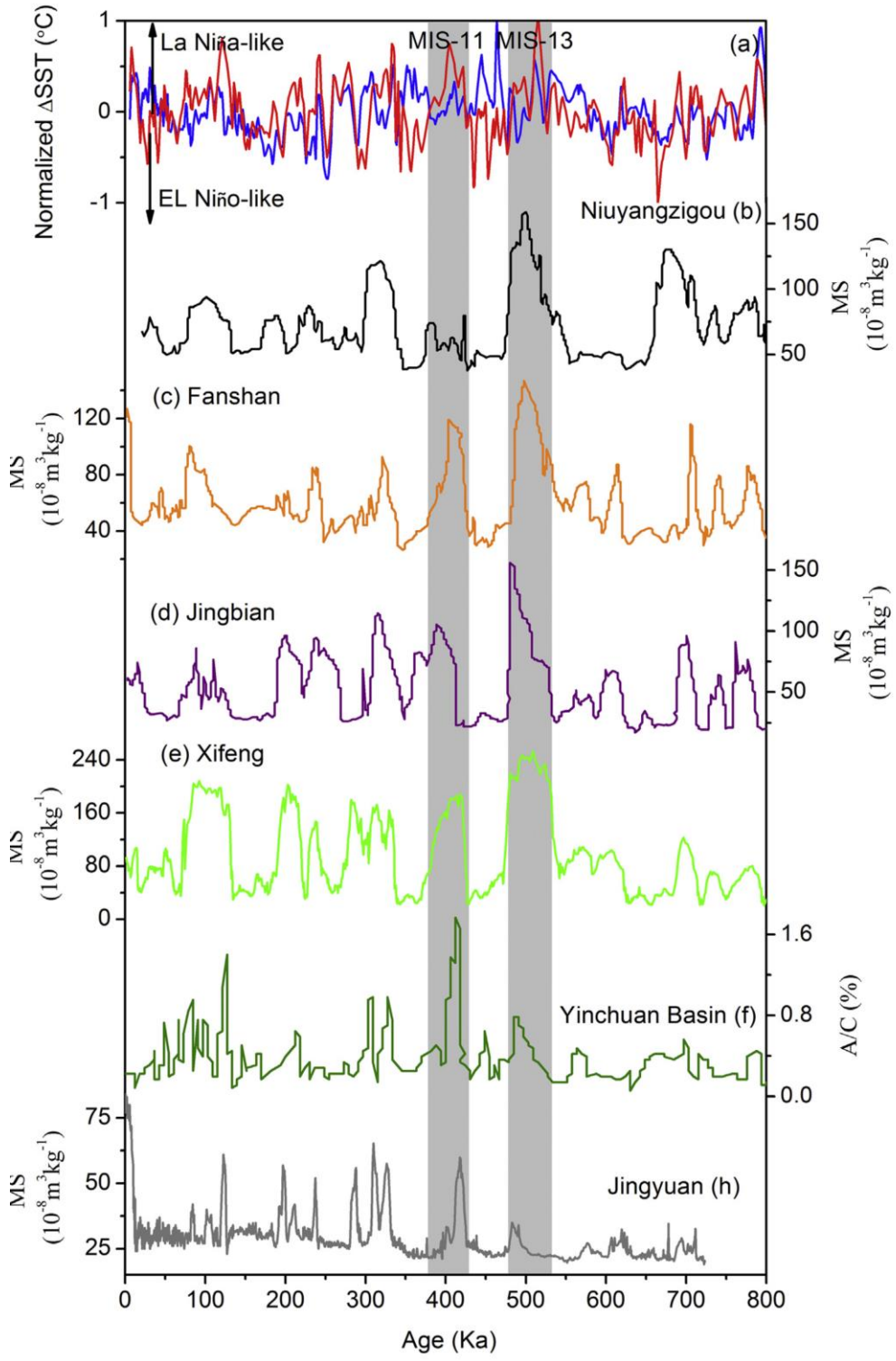

Figure 3. The comparison of zonal SST gradients (DSST) between MD97-2140 (de Garidel-Thoron et al., 2005) and RC11-210 (Pisias and Rea, 1988) (red curve), MD97-2140 and ODP846 (blue curve) (a) with magnetic susceptibility records in Niuyangzigou section (Lin et al., 2017) (b), Fanshan section (Xiong et al., 2001) (c), Jingbian section (Ding et al., 2005) (d), Xifeng section (Guo et al., 2009) (e), Jingyuan section (Sun et al., 2006a) (h) and pollen records in Yinchuan Basin (Li et al., 2017a) (f). Gray frame denote the proxies for which MIS-13 and MIS-11 are contrasted in the paper. (For interpretation of the references to color in this figure legend, the reader is referred to the Web version of this article.)

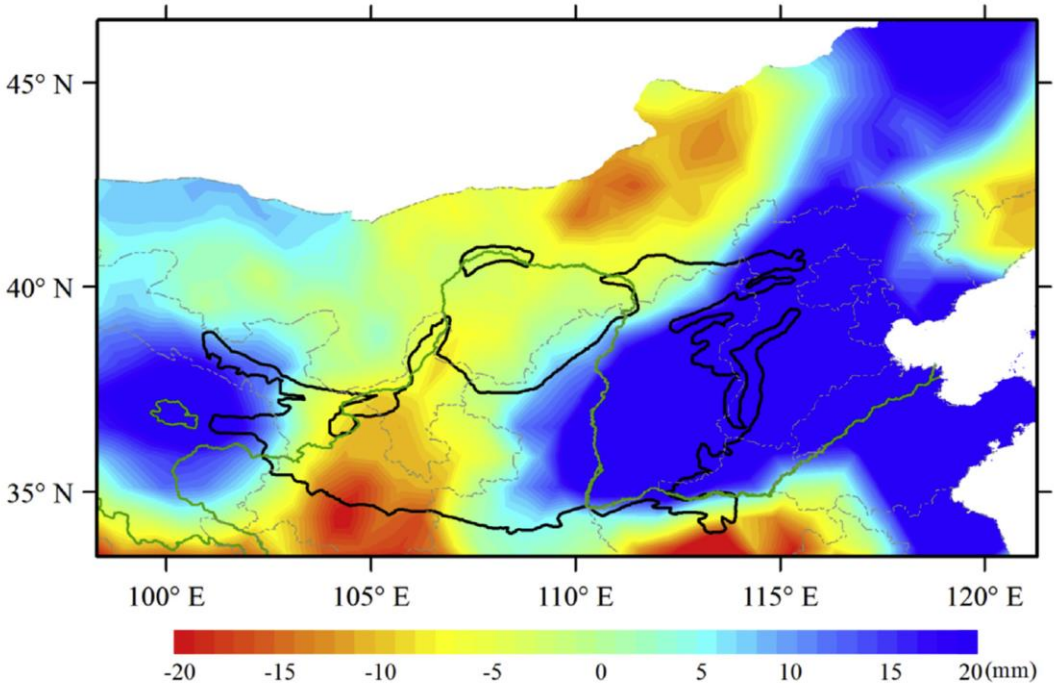

Figure. 4. Modern summer average precipitation spatial distribution difference (mm/day) between all the strong La Nina years and weak La Ni ~ na years from 1961 to 2014. The strong La ~Nina years and weak La Nina years are de ~ fined by Mei index and are ranked by the value of winter SST (https://www.esrl.noaa.gov/psd/enso/climaterisks/years/top24enso.html); the precipitation data is obtained from 824 observational stations in China for the period 1961 to 2014, archived and updated by the China Meteorological Administration (http:// data.cma.cn/data/cdcdetail/dataCode/SURF CLI CHN MUL DAY V3.0.html).

2. 地球上最古老的花岗质岩石是硅质岩浆喷发后留下的富晶体的岩浆房

翻译人：冯婉仪 fengwy@sustech.edu.cn

Laurent O, Björnsen J, Wotzlaw J F, et al. ***Earth' s earliest granitoids are crystal-rich magma reservoirs tapped by silicic eruptions****[J].* ***Nature Geoscience****, 2020, 13: 163-169.*

摘要：地球最古老的大陆地壳主要是由英云闪长岩-奥长花岗岩-花岗闪长岩（TTG）系列的花岗质岩石组成。TTGs 的地球化学多样性归因于岩浆可在几种地球动力学背景下形成，即从大洋高原的低压分异作用到汇聚板块边缘的镁铁质地壳的高压熔融。这些解释是假设岩浆从源区形成后至完全结晶过程中，TTGs 的全岩成分没有发生变化。然而，显生宙同时期形成的深成岩体与硅质火山岩在结构和化学上的互补性表明，晶体-液体分离会影响长英质岩浆的地球化学成分。在这里，我们证明了南非古太古代（约 34.56 亿年）的 TTG 深成岩体不能代表熔体的成分，它代表了硅质火山岩喷发后留下的古老的富晶体的岩浆房，通过高精度的 U-Pb 年代学研究发现这些 TTG 深成岩体与酸性火山岩在百万年的尺度下可能是同时代的。大多数奥长花岗岩的化学特征通常被认为是玄武岩高压熔融产生的熔体，但它反映了斜长石斑晶的堆晶作用以及晶体间的熔体已经以硅质火山岩喷发的形式离开这个体系。我们的研究结果表明，TTGs 的整体成分的多样性可能是由玄武岩熔融和/或结晶形成的单一的英云闪长岩质岩浆在小于 40 km 深度的上地壳分异形成的。这些结果要求一个统一的模型，地壳内 TTG 岩浆的形成导致了冥古宙-太古代大陆成核。

ABSTRACT: Granitoids of the tonalite–trondhjemite–granodiorite (TTG) series dominate Earth's earliest continental crust. The geochemical diversity of TTGs is ascribed to several possible geodynamic settings of magma formation, from low-pressure differentiation of oceanic plateaus to high-pressure melting of mafic crust at convergent plate margins. These interpretations implicitly assume that the bulk-rock compositions of TTGs did not change from magma generation in the source to complete crystallization. However, crystal–liquid segregation influences the geochemistry of felsic magmas, as shown by the textural and chemical complementarity between coeval plutons and silicic volcanic rocks in the Phanerozoic Eon. We demonstrate here that Paleoarchean (ca. 3,456 million years old) TTG plutons from South Africa do not represent liquids but fossil, crystal-rich magma reservoirs left behind by the eruption of silicic volcanic rocks, being possibly coeval at the

million-year scale as constrained by highprecision uranium–lead geochronology. The chemical signature of the dominant trondhjemites, conventionally interpreted as melts generated by high-pressure melting of basalts, reflects the combined accumulation of plagioclase phenocrysts and loss of interstitial liquid that erupted as silicic volcanic rocks. Our results indicate that the entire compositional diversity of TTGs could derive from the upper crustal differentiation of a single, tonalitic magma formed by basalt melting and/or crystallization at < 40 km depth. These results call for a unifying model of Hadean–Archean continent nucleation by intracrustal production of TTG magmas.

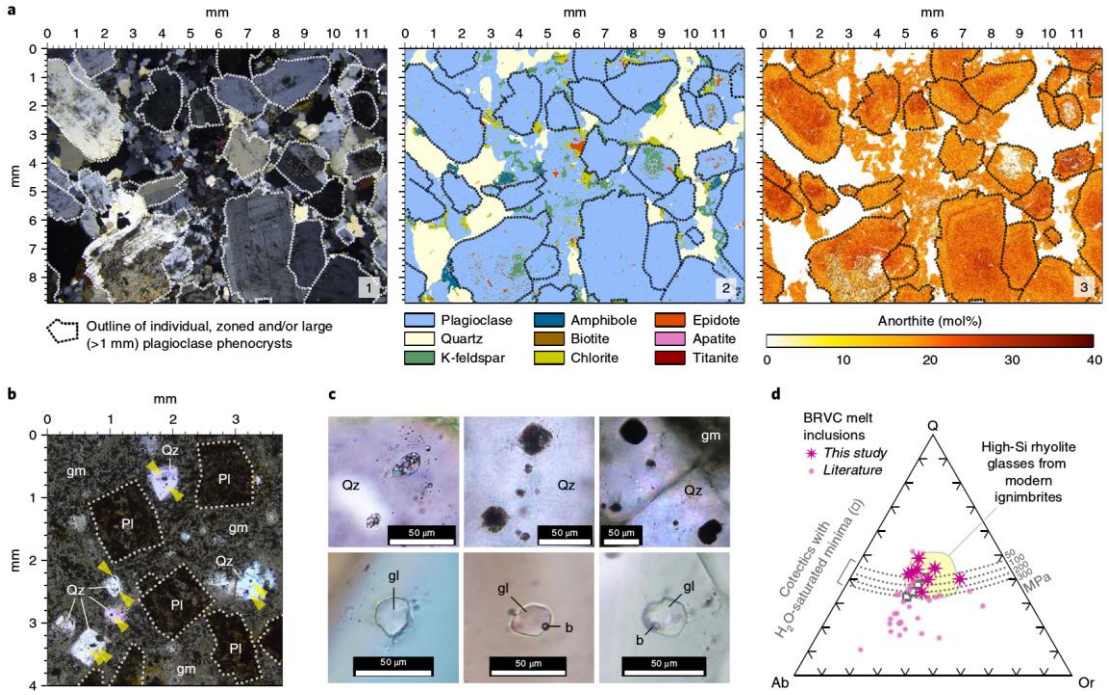

Figure 1. The Paleoarchean Barberton TTG plutons and BRVC volcanic rocks are, respectively, crystal-rich and liquid-rich magmatic units. a, The same region of a trondhjemite sample (JB17-C2a) imaged by optical microscopy with crossed polars (panel 1) and SEM-EDS spectral images, including phase map (panel 2) and plagioclase compositional map (panel 2). In panel 2, some plagioclase phenocryst cores altered to sericite are incorrectly assigned as K-feldspar. b, Photomicrograph showing the phyric texture of a volcanic sample from the BRVC (JB17-F8) with altered groundmass (gm), plagioclase (Pl) and pristine quartz (Qz) containing melt inclusions (arrows). c, Photomicrographs showing representative examples of the BRVC melt inclusions, unheated (top row) and after homogenization (bottom row; gl = glass; b = gas bubble). d, Normative albite (Ab)-quartz (Q)-orthose (Or) triangle showing the normative composition of the BRVC melt inclusions compared with the H_2O-saturated temperature minima in the haplogranitic system[50] and high-silica rhyolitic glass from modern ignimbrites (compiled by ref. [51]).

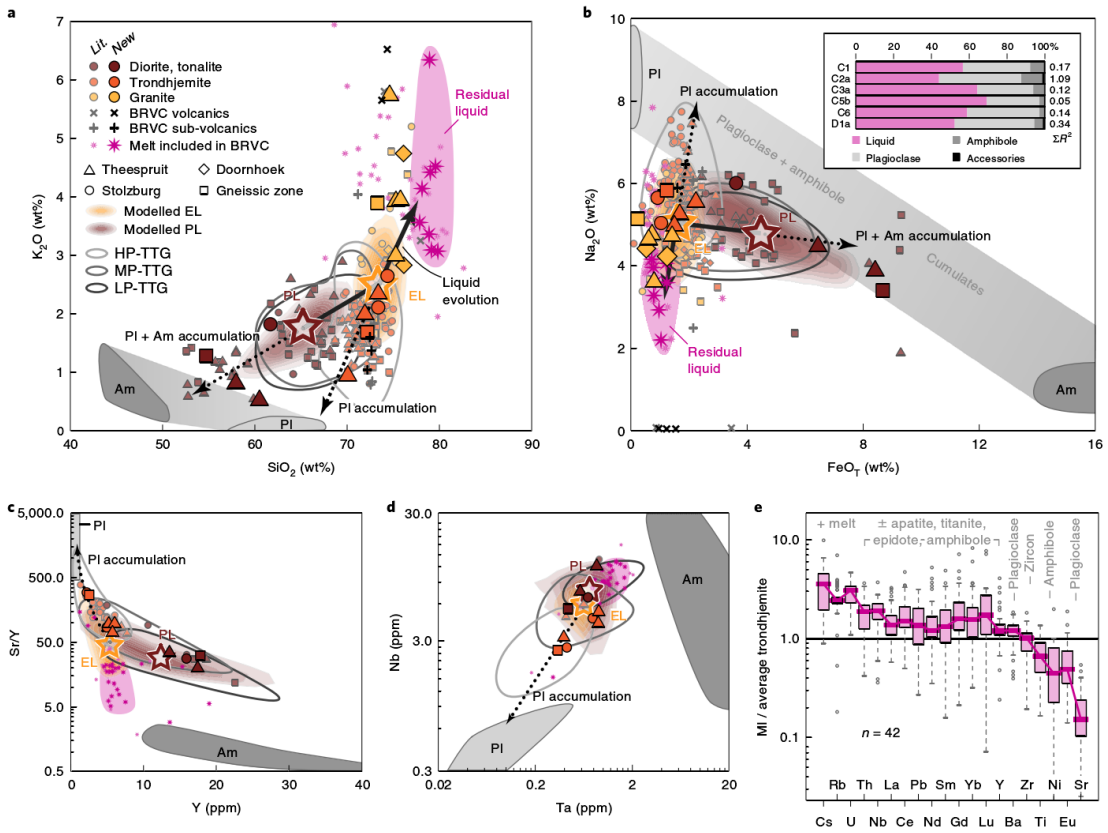

Figure 2. Geochemical evidence that the compositional range of TTGs can be explained by crystal–liquid segregation associated with the differentiation of a single parental liquid. a-d, Diagrams of K_2O versus SiO_2 (a), Na_2O versus FeOt (b), Sr/Y versus Y (c) and Nb versus Ta (d) showing the compositions of bulk samples and homogenized BRVC melt inclusions (Lit., literature data[8,20,25-27]; New, this study) together with amphibole (Am) and plagioclase (Pl) in the plutons. The compositions of PL and EL were obtained by stochastic mass-balance modelling (Methods). The coloured fields contain 95% of the trial runs; darker shading means higher point density; stars indicate the average composition. The fields for TTG groups are after ref. [11]. The top-right inset in b shows the results of least-square fitted mass balance of phase proportions in bulk trondhjemite samples (Methods; ΣR^2 = sum of squared residuals). e, Box-andwhisker plot (horizontal line indicates the median; boxes indicate first to third quartiles) of the distribution of selected element contents in the BRVC melt inclusions (this study and ref. [25]) normalized to average trondhjemites.

3. 始新世-渐新世转换期间大洋鱼类生产力与多样性并无显著变化

翻译人：蒋晓东 jiangxd@sustech.edu.cn

Sibert, E. C., Zill, M. E., Frigyik, E. T et al., ***No state change in pelagic fish production and biodiversity during the Eocene–Oligocene transition****. Nature Geoscience. [J] (2020) 13, 238-242.*

摘要：始新世-渐新世边界（~33.9 Ma）被认为是以显著的南极冰川作用增强和大洋生产力升高为标志的地球系统状态变化。本研究通过研究全球范围 7 个深海钻孔的鱼牙化石，定量化分析鱼类生产力和多样性对这次事件的响应。研究发现鱼牙化石沉积速率（鱼类生产力指标）并未同步于始新世-渐新世转换的趋势。在南大洋和太平洋涡流区的鱼牙化石沉积速率低于赤道和大西洋区一个数量级，表明南大洋在始新世-渐新世转换前后并不是一个鱼类高生产力的生态系统。这期间鱼牙的形态多样性和聚集结构仍然保持稳定，这表明开放大洋鱼类的生态角色或者多样性并未改变。始新世-渐新世边界是一个全球气候事件，而它对大洋鱼类的影响相对柔和的。我们的结果支持近期关于鲸鱼和磷虾的多样性研究，这表明普遍归因于始新世-渐新世转换的大洋生态系统重建很可能发生在在渐新世晚期或者中新世。

ABSTRACT： The Eocene/Oligocene (E/O) boundary (~33.9 million years ago) has been described as a state change in the Earth system marked by the permanent glaciation of Antarctica and a proposed increase in oceanic productivity. Here we quantified the response of fish production and biodiversity to this event using microfossil fish teeth (ichthyoliths) in seven deep-sea sediment cores from around the world. Ichthyolith accumulation rate (a proxy for fish biomass production) shows no synchronous trends across the E/O. Ichthyolith accumulation in the Southern Ocean and Pacific gyre sites is an order of magnitude lower than that in the equatorial and Atlantic sites, demonstrating that the Southern Ocean was not a highly productive ecosystem for fish before or after the E/O. Further, tooth morphotype diversity and assemblage composition remained stable across the interval, indicating little change in the biodiversity or ecological role of open-ocean fish. While the E/O boundary was a major global climate-change event, its impact on pelagic fish was relatively muted. Our results support recent findings of whale and krill diversification suggesting that the pelagic ecosystem restructuring commonly attributed to the E/O transition probably occurred much later, in the late Oligocene or Miocene.

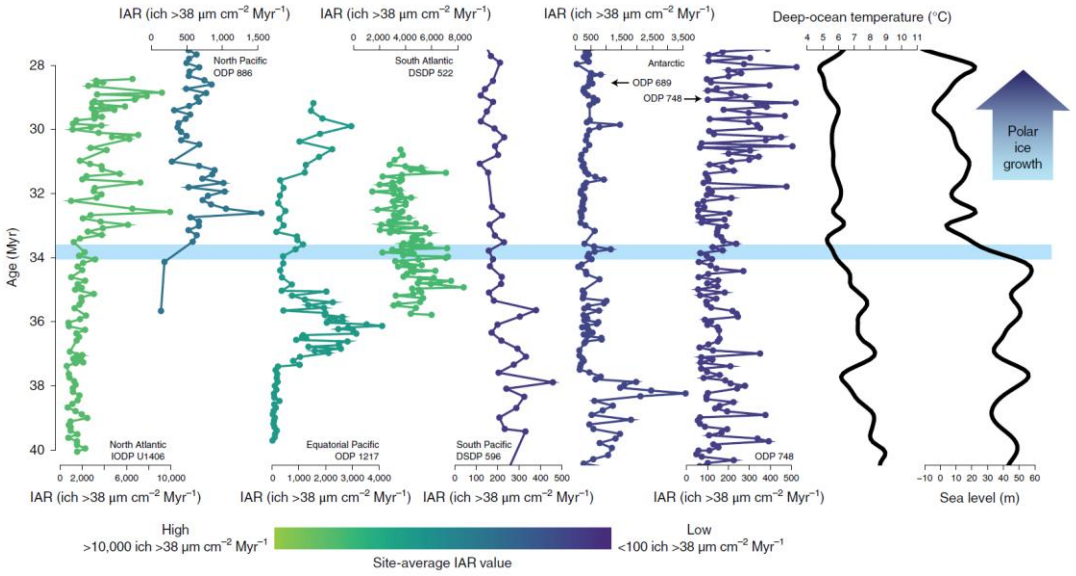

Figure 1. IARs from sites included in this study, arranged approximately from northernmost to southernmost latitude, show no significant trends across the E/O (light-blue horizontal line). Sites are coloured on the basis of their average productivity throughout the interval, which spans nearly two orders of magnitude, with higher fish production sites in green and lower fish production sites in blue. IAR is in the units ichthyoliths >38 µm cm^{-2} Myr^{-1}. The two right-most curves are showing global temperature and sea level as reported by Cramer et al.

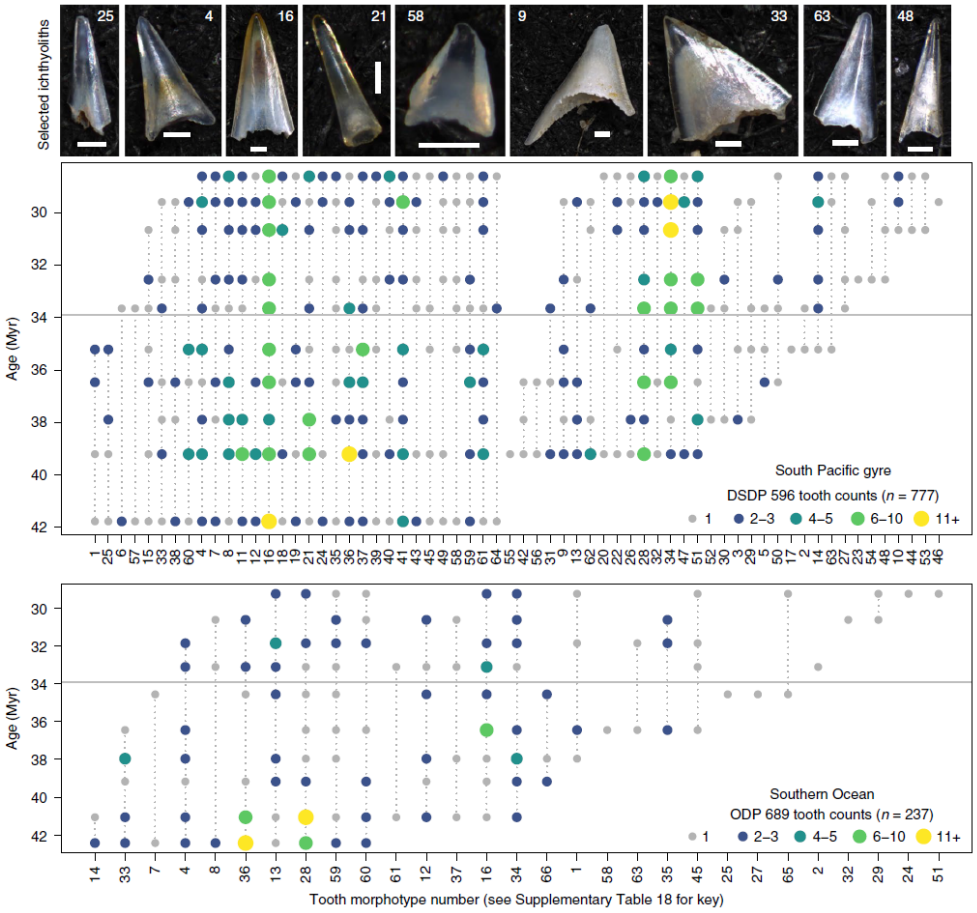

Figure 2. Range charts from DSDP Site 596 (top) and ODP Site 689 (bottom) showing the occurrences of each of the 66 tooth morphotypes described in this study, ordered on the x axis by first occurrence within each site. The size

and colour of the dot refers to the count abundance of that morphotype within the sample's time slice. The grey horizontal line is the E/O boundary. The x-axis numbers and top-row numbers refer to the morphotypes as listed in Supplementary Table 18. Images in the top row are representative tooth forms (numbers refer to the morphotype), and the scale bars represent 100 μm.

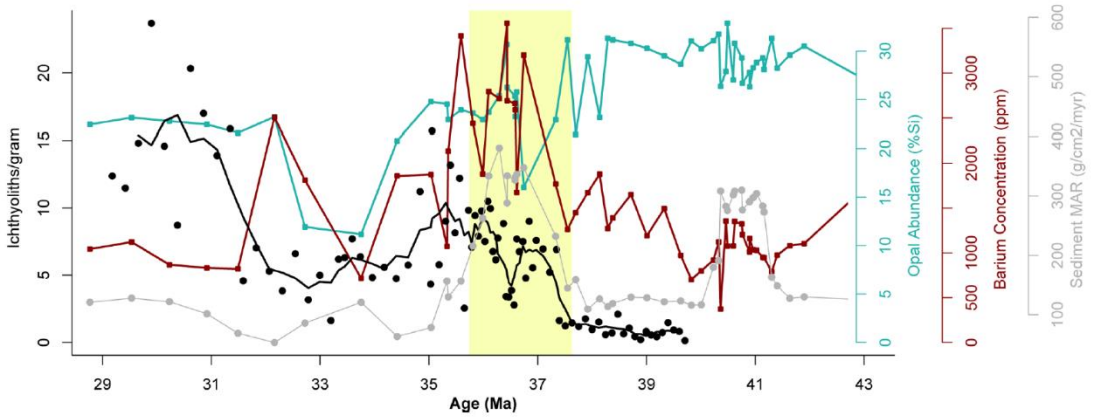

Figure 3. A comparison of sediment mass accumulation rate (gray) with the raw concentration values for ichthyoliths per gram (black), barium concentration (parts per million) and opal abundance (% silica) for ODP Site 1217. The Yellow box highlights a two-million year period of elevated sediment MAR that is associated with an increase in the concentration of ichthyoliths and barium but not silica.

4. 增生后沉积物对海洋磁异常的影响

翻译人：李园洁 liyj3@sustech.edu.cn

Granot R, Dyment J. ***The influence of post-accretion sedimentation on marine magnetic anomalies[J]. Geophysical Research Letters****, 2019, 46(9): 4645-4652.*

摘要：海洋磁异常对于海底扩张和被动陆缘海底与陆壳之间的过渡带的研究非常重要。但是，显著的增生后沉积物会扰乱洋壳的热状态，从而改变其剩余磁化强度。为了研究沉积物和洋壳的磁化强度之间的关系，我们建立了一系列具有不同沉积过程的热剩磁正演模型，并与南大西洋南部早白垩纪的观测资料进行比较。我们的模拟结果表明，根据增生后沉积物的厚度，可部分或完全去除掉喷出玄武岩的剩余磁化强度。因此，在覆盖厚沉积物的洋壳上观测到的典型的长波长海平面磁异常几乎完全是由较深磁化层产生的。

ABSTRACT： Marine magnetic anomalies are a critical observation used to investigate seafloor spreading and the transition between oceanic and continental crust at passive margins. However, pronounced post-accretion sedimentation disturbs the thermal state of the crust and therefore alters its remanent magnetization. To study the link between sedimentation and magnetization of the oceanic crust, we built a series of thermomagnetic forward models coupled with different sedimentation histories. We test our approach against observations from the early Cretaceous southern South Atlantic Ocean. Our simulations suggest that, depending on the thickness of post-accretion sediments, the remanent magnetization of the extrusive basalts is partly or completely removed. Therefore, the typical long-wavelength sea surface marine magnetic anomalies observed above oceanic crust covered by a thick sedimentary pile is almost entirely generated by the magnetization of the deeper crustal layers.

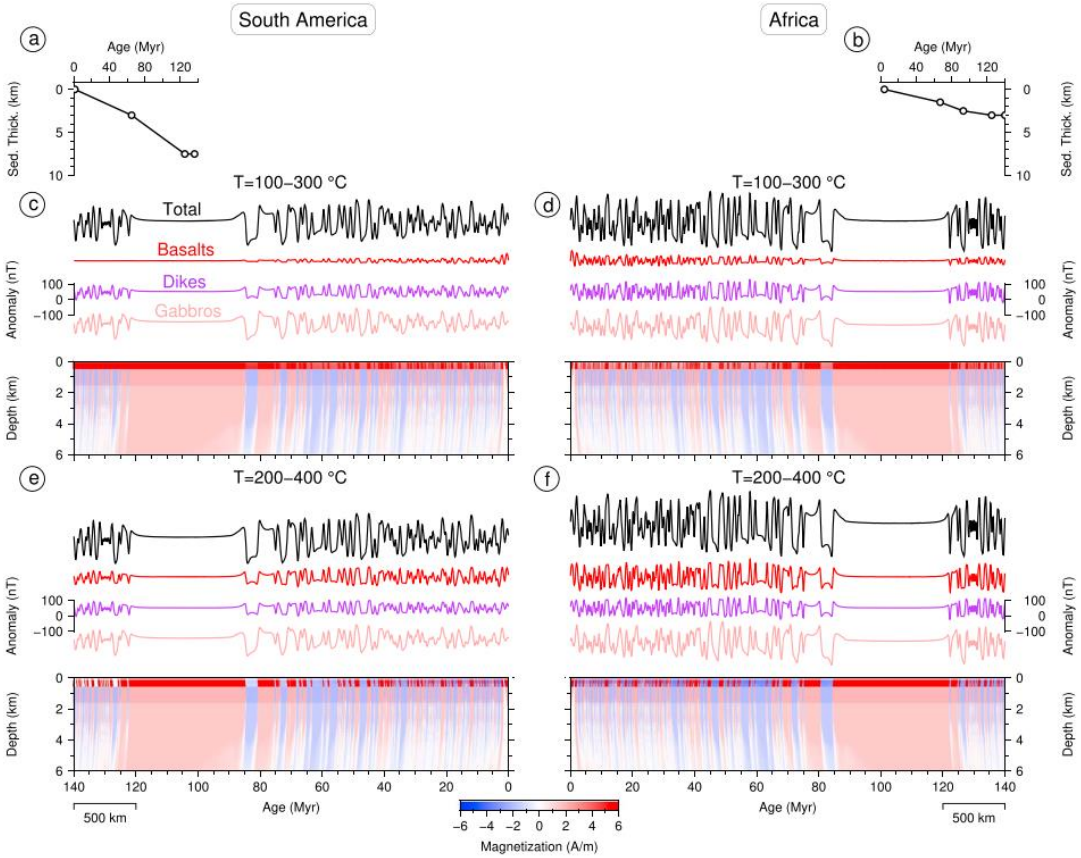

Figure 1. Results from the thermomagnetic forward modeling. (a, b) Sedimentation rate curves of the investigated Cretaceous-aged South American (a; Morales et al., 2017) and African (b; Dressel et al., 2015) southern South Atlantic flanks that were incorporated into the models. (c–f) Magnetization grids and the resultant magnetic anomalies. The anomalies are computed separately for the gabbro, sheeted dike and basalt layers and are shown in light red, purple, and red, respectively. The sum of these three contributions is shown in black. In all models, the blocking temperatures for the sheeted dikes and gabbros range between 400 and 580 °C. The blocking temperatures of the basalts were simulated with ranges of 100 to 300 °C (c, d) and 200 to 400 °C (e, f). These models were constructed using constant 7- and 10-km depths for the African and South American top of the basalt layer, respectively.

5. 地球早期的硅酸盐发电机

翻译人：柳加波

Stixrude L, Scipioni R, Desjarlais M P. ***A silicate dynamo in the early Earth****[J]. Nature communications, 2020, 11(1): 1-5.*

摘要：地球磁场至少运转了 34 亿年，但我们仍然不清楚古代磁场是如何产生的。地球早期的内核被熔融的硅酸盐层包裹，这种基底岩浆海洋可能已经存在超过十亿年。在这里，我们使用基于密度泛函理论的分子动力学模型，在压力 100-140 GPa 和温度 4000-6000K 的基底岩浆海洋条件下，预测硅酸盐液体的电导率。我们发现电导率超过 10,000 S/m，这是低压和低温条件下硅酸盐液体电导率的 100 倍以上。根据我们的结果，计算得出的磁雷诺数(magnetic Reynolds number)超过了发电机活动的阈值，并且磁场强度与太古宙古磁记录中观察到的相似。因此，我们认为太古宙地磁场是由基底岩浆海产生的。

ABSTRACT： The Earth's magnetic field has operated for at least 3.4 billion years, yet how the ancient field was produced is still unknown. The core in the early Earth was surrounded by a molten silicate layer, a basal magma ocean that may have survived for more than one billion years. Here we use density functional theory-based molecular dynamics simulations to predict the electrical conductivity of silicate liquid at the conditions of the basal magma ocean: 100–140 GPa, and 4000–6000 K. We find that the electrical conductivity exceeds 10,000 S/m, more than 100 times that measured in silicate liquids at low pressure and temperature. The magnetic Reynolds number computed from our results exceeds the threshold for dynamo activity and the magnetic field strength is similar to that observed in the Archean paleomagnetic record. We therefore conclude that the Archean field was produced by the basal magma ocean.

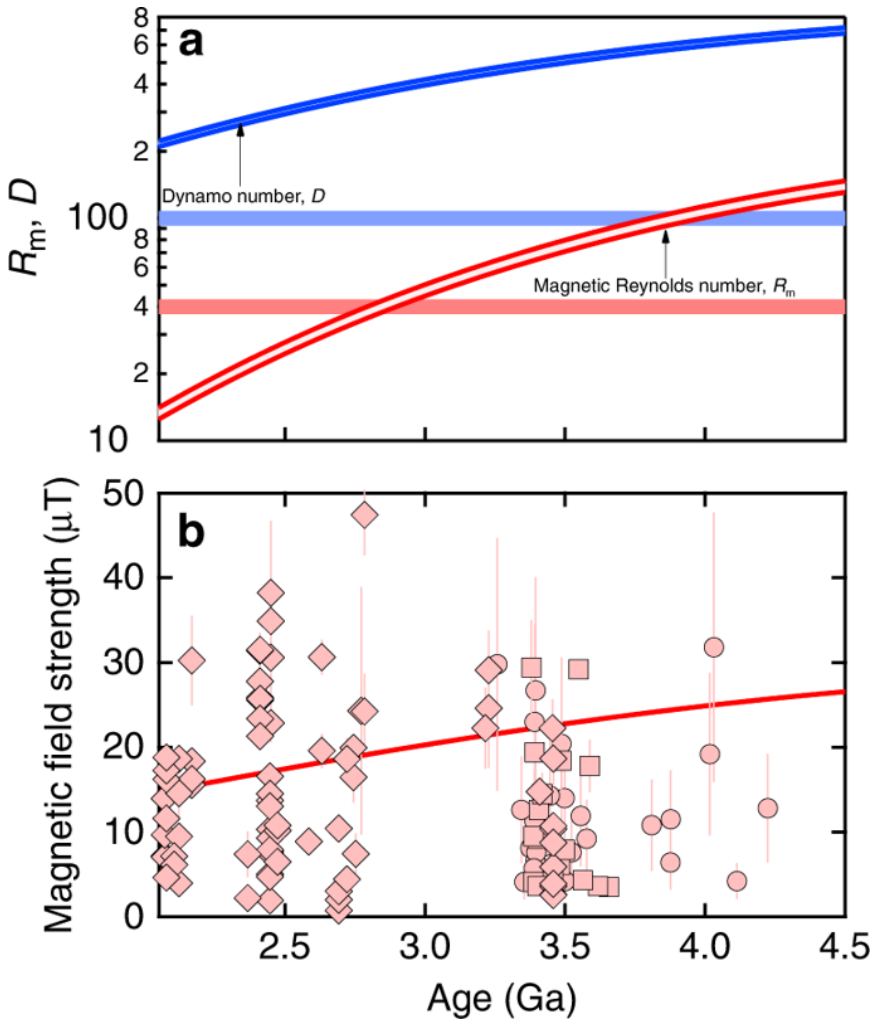

Figure 1. Magnetic Reynolds number and magnetic field strength. a The magnetic Reynolds number (red) and Dynamo number (blue) computed from our electrical conductivity results and thermal evolution model with shading indicating the difference between low-spin (top of range) and high-spin (bottom of range) results compared with the respective critical values of Rm = 40 and D = 100 (thick horizontal lines). b Magnetic field strength computed from our model (red line) compared with paleomagnetic data: diamonds from the PINT database, and circles (Thellier–Coe method) and squares (565C method) from zircons. We note that the evidence of a field prior to the oldest whole-rock PINT data at 3.45 Ga relies on the single-crystal zircon results, which have been questioned as not deriving from a primary magnetic carrier.

6. 湖泊沉积物中碳酸盐岩的稳定氧碳同位素作为古洪水的代用指标

翻译人：郑威　11930589@mail.sustech.edu.cn

Kämpf L, Plessen B, Lauterbach S, et al. ***Stable oxygen and carbon isotopes of carbonates in lake sediments as a paleoflood proxy****[J].* ***Geology****, 2020, 48(1): 3-7.*

摘要：湖泊沉积物越来越多地被视为记录古洪水的可靠档案。除了已建立的包括碎屑层厚度、化学成分、粒度等洪水代用指标外，我们探究了稳定氧碳同位素数据作为基岩为碳酸盐岩的流域中湖泊的古洪水代用指标。在奥地利Mondsee湖的案例研究中，我们整合了近端和远端收集的高分辨率沉积物和有纹层的湖泊沉积物钻孔的稳定同位素分析以研究洪水触发的碎屑沉积物的通量。首先，我们证明了公元2011-2013年间径流量、碎屑沉积物通量与沉积物记录的同位素数值之间的关系，包括了22个事件，其径流量日（小时）峰值为10（24）m^3s^{-1}到79（110）m^3s^{-1}。远端收集的沉积物中减弱的稳定同位素数值的峰值很好的反映了3-10倍少的洪水触发的碎屑沉积物在远端沉积。接下来，我们表明，沉积物记录的1988–2013年间所有9层洪水触发的碎屑层与内生的方解石相比有较高的同位素数值。此外，尽管有两个径流事件没有造成可见的碎屑层沉积也通过较高的同位素数值显示出来。同位素数据的经验阈值可以估算大多数洪水的强度，尽管在某些案例中洪水强度因为区域影响导致了过高的同位素数值而被高估了。因此，我们提出了一个稳定同位素作为重建洪水频率的可靠工具的概念的证明，但是它依然存在一些甚至是对洪水强度的估计的局限性。

ABSTRACT： Lake sediments are increasingly explored as reliable paleoflood archives. In addition to established flood proxies including detrital layer thickness, chemical composition, and grain size, we explore stable oxygen and carbon isotope data as paleoflood proxies for lakes in catchments with carbonate bedrock geology. In a case study from Lake Mondsee (Austria), we integrate high-resolution sediment trapping at a proximal and a distal location and stable isotope analyses of varved lake sediments to investigate flood-triggered detrital sediment flux. First, we demonstrate a relation between runoff, detrital sediment flux, and isotope values in the sediment trap record covering the period 2011–2013 CE including 22 events with daily (hourly) peak runoff ranging from 10 (24) $m^3 s^{-1}$ to 79 (110) $m^3 s^{-1}$. The three- to ten-fold lower flood-triggered detrital sediment deposition in the distal trap is well reflected by attenuated peaks in the stable isotope values of trapped sediments. Next, we show that all nine flood-triggered detrital layers deposited in a sediment record from 1988

to 2013 have elevated isotope values compared with endogenic calcite. In addition, even two runoff events that did not cause the deposition of visible detrital layers are distinguished by higher isotope values. Empirical thresholds in the isotope data allow estimation of magnitudes of the majority of floods, although in some cases flood magnitudes are overestimated because local effects can result in too-high isotope values. Hence we present a proof of concept for stable isotopes as reliable tool for reconstructing flood frequency and, although with some limitations, even for flood magnitudes.

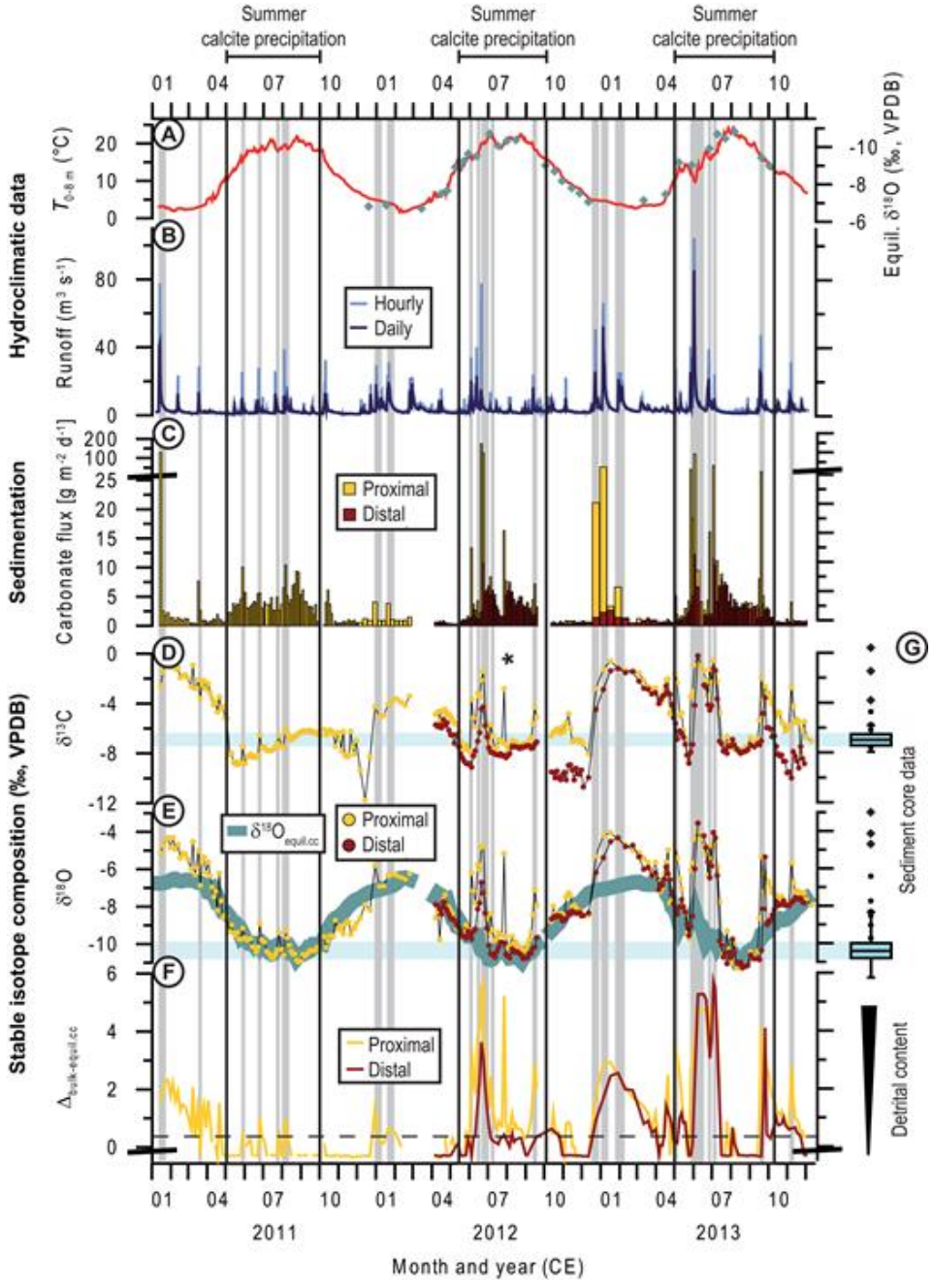

Figure 1. Three years of monitoring data on hydroclimatic variables and trapped sediment at Lake Mondsee (Austria). Gray vertical bars mark flood-triggered peaks in sediment flux and isotopes. (A)

Epilimnion (0–8 m depth) water temperature (red line) and calculated equilibrium $\delta^{18}O$ (green diamonds) of endogenic calcite (Appendices DR1 and DR2 [see footnote 1]). (B) River runoff. (C) Carbonate flux. Note change in vertical scale above 25 g m^{-2} d^{-1}. (D) Bulk $\delta^{13}C$ in sediment. Star marks one isotope peak not correlated to runoff due to gap in runoff data. (E) Bulk $\delta^{18}O$ in sediment with calculated endogenic calcite $\delta^{18}O$ ($\delta^{18}O_{equil.cc}$) (Appendix DR2). (F) Differences between measured and calculated endogenic $\delta^{18}O$ ($\Delta_{bulk–equil.cc}$). Horizontal dashed line marks the minimum difference between measured $\delta^{18}O$ and $\delta^{18}O_{equil.cc}$ (0.5 per mil). (G) Bulk $\delta^{13}C$ and $\delta^{18}O$ of calcite layers (box plots, n = 17), microscopic detrital layers (dots, n = 9), and macroscopic detrital layers (diamonds; n = 3). “Proximal” and “distal” indicate proximal and distal sediment traps, respectively (see Fig. 1). VPDB—Vienna Peedee belemnite.

7. 西太平洋赤道远洋沉积物中的生物地球化学剩磁

翻译人：王敦繁

Tarduno J A, Tian W, Wilkison S. ***Biogeochemical remanent magnetization in pelagic sediments of the western equatorial Pacific Ocean[J]. Geophysical Research Letters,*** *1998, 25(21):3987-3990.*

摘要：远洋沉积物中载有的古地磁信息是研究地质历史时期地磁场演变的的重要资料来源。然而，关于这些沉积物获得剩磁的过程和机制仍然存在很大的不确定性。在此，我们探讨了西太平洋赤道沉积物深处(ODP Site805)形成的生物磁铁矿对剩余磁化强度的贡献。结果表明在铁氧化还原边界附近发现的生物磁铁矿具有天然的剩余磁化。由于生物磁铁矿的生产与保存与沉积物的地球化学分带有关，所以我们把这种剩磁称为生物地球化学剩磁。研究数据表明，一些远洋沉积物在经历了后沉积过程通过碎屑磁性颗粒获得剩磁后，仍可继续获得明显的生物地球化学剩磁。

ABSTRACT: Paleomagnetic data from pelagic sediments are an important source of information on the history of the geomagnetic field. However, fundamental uncertainties about how these sediments acquire their magnetizations remain. Here we address whether biogenic magnetite, formed at depth within the sediments, can contribute to remanent magnetizations. In sediments of the western equatorial Pacific Ocean (ODP Site805), biogenic magnetite found near the Fe-redox boundary carries a natural remanent magnetization. Because the production of biogenic magnetite is tied to the geochemical zonation of the sediments, we call this magnetization a biogeochemical remanence. These data indicate that some pelagic sediments can continue to acquire remanence significantly after the post-depositional lock-in of detrital magnetic grains.

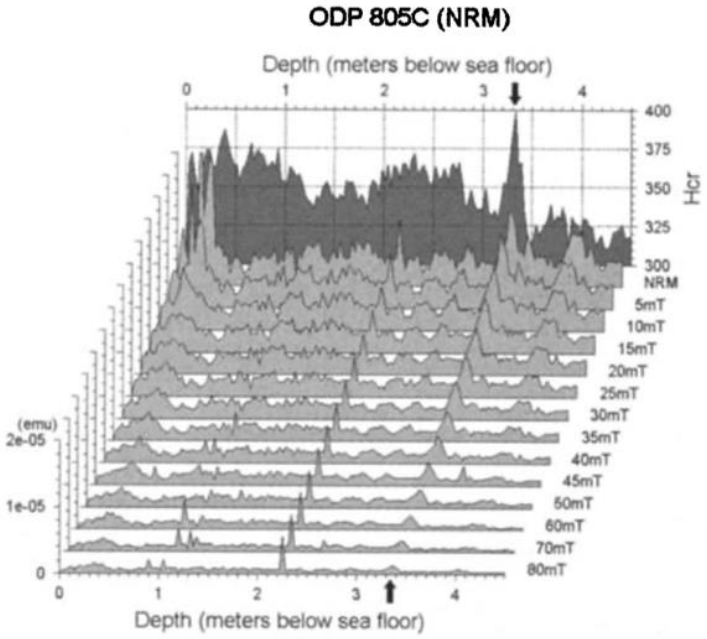

Figure 1. Site 805C alternating field demagnetization of natural remanent magnetization (NRM)

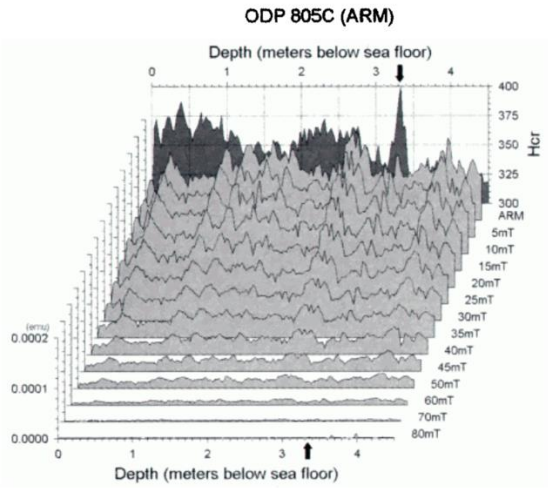

Figure 2. Site 805C alternating field demagnetization of anhysteretic remanent magnetization (ARM)

8. 中国西南地区石笋记录的末次冰期-间冰期以来亚洲夏季风变化

翻译人：杨会会 11849590@mail.sustech.edu.cn

Wu Y, Li T Y, Yu T L, et al. ***Variation of the Asian summer monsoon since the last glacial-interglacial recorded in a stalagmite from southwest China[J].Quaternary Science Reviews,*** *2020, 243:106261.*

摘要：大量研究支持亚洲夏季风区的气候变化和北半球高纬地区、南半球之间存在紧密联系，但相关机制仍然存疑。尽管石笋氧同位素记录在轨道-千百年尺度古气候变化重建方面已经展示出了很高的价值，但石笋碳氧同位素值的意义还存在一定争议。在本文中，我们用高分辨率 230Th 定年的中国西南地区石笋记录，通过耦合碳氧同位素技术，重建了末次间冰期以来（3.6-118.1 ka BP）亚洲夏季风和区域水文条件的变化。结果表明：1. 东亚夏季风和印度夏季风在轨道尺度上是同期变化的，响应北半球夏季太阳辐照量和高纬气候的变化；通过马斯克林高压和索马里急流，南极洲气温变化和亚洲夏季风之间存在遥相关关系。2. 在 MIS 5d 期间，Yangzi 洞石笋氧同位素值接近 1.5‰，高于 MIS 2 末次冰盛期阶段的值,这是因为东亚夏季风和印度夏季风水汽来源不同引起的同位素组成差异，以及季风环流动力差异。3. MIS 3 到 MIS 2 期间，亚洲夏季风呈现一种“阶梯式”减弱的形态，和北半球夏季辐照量减少及全球冰量增加相一致。4. 石笋碳同位素值变化揭示了局部水文条件变化，与氧同位素值反映的气候变化紧密相关。由温度确定的有效湿度、蒸发量和降水量，共同主导区域水文条件。有效湿度变化，通过影响地表生物量和土壤 CO_2 产量，记录在石笋碳同位素中。

ABSTRACT: A number of studies proposed a close link between the climate changes in the Asian summer monsoon(ASM), the Southern Hemisphere (SH), and high latitudes of the Northern Hemisphere (NH). But the mechanisms is still an open question. Although speleothems $d^{18}O$ records have displayed excellent values in the reconstruction of paleoclimate change at centennial - millennial to orbital timescales, the significance of speleothems $d^{18}O$ and $d^{13}C$ is still debatable. Here, a high-precise ^{230}Th dated stalagmite from southwestern China was used to reconstruct the changes of ASM and regional hydrological conditions since the last interglacial (3.6e118.1 ka BP) by the coupled $d^{18}O$ and $d^{13}C$. We found: (1) The EASM and ISM are synchronous changing on the orbital timescale, responding to the change of North Hemisphere summer insolation (NHSI) and high latitude climate change. There is a teleconnection between Antarctic temperature change and ASM through the Mascarene High and the

Somali Jet. (2) During MIS 5d, the stalagmite $d^{18}O$ in Yangzi Cave is nearly 1.5‰ higher than that in MIS 2, the maximum of last glacial. This should be attributed to the different isotopic compositions in moisture source of ISM and EASM, and the dynamic changes of monsoon circulations. (3) From MIS 3 to MIS 2, the ASM showed a "stepped" pattern in weakening, consistent with the decreasing NHSI and increasing global ice volume. (4) The changes in stalagmite $d^{13}C$ indicated the changes of local hydrological conditions and closely correlated with climate changes revealed by stalagmite $d^{18}O$. The effective humidity, which determined by temperature, evaporation, and precipitation, dominated the regional hydrological conditions. The change of effective humidity recorded in stalagmite $d^{13}C$ by influencing surface biomass and soil CO_2-production.

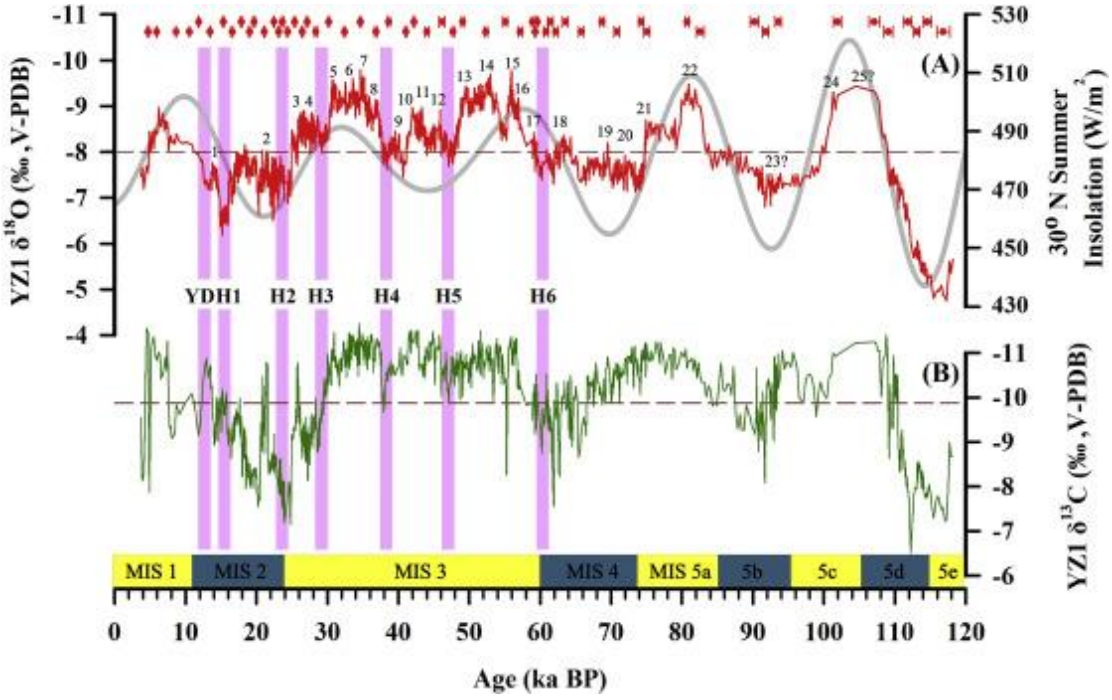

Figure 1. YZ1 stalagmite $d^{18}O$ (A) and $d^{13}C$ (B) records; red dots are the depth and age of the U-Th dating samples, and the error bars indicate the dating error (±2s). The brown dotted lines show the average values of $d^{18}O$ (8.0‰) and $d^{13}C$ (9.9‰), respectively. The gray curve shows the 30°N summer insolation (Berger and Loutre, 1991). The pink vertical bars indicate YD and H events (Heinrich, 1988); the Arabic numbers indicate the D-O event (Dansgaard et al., 1993). The yellow and cyan bands along X-axis indicate Marine Isotope Stages (MIS) (Lisiecki and Raymo, 2005; NEEM Community Members, 2013). (For interpretation of the references to color in this figure legend, the reader is referred to the Web
version of this article.)

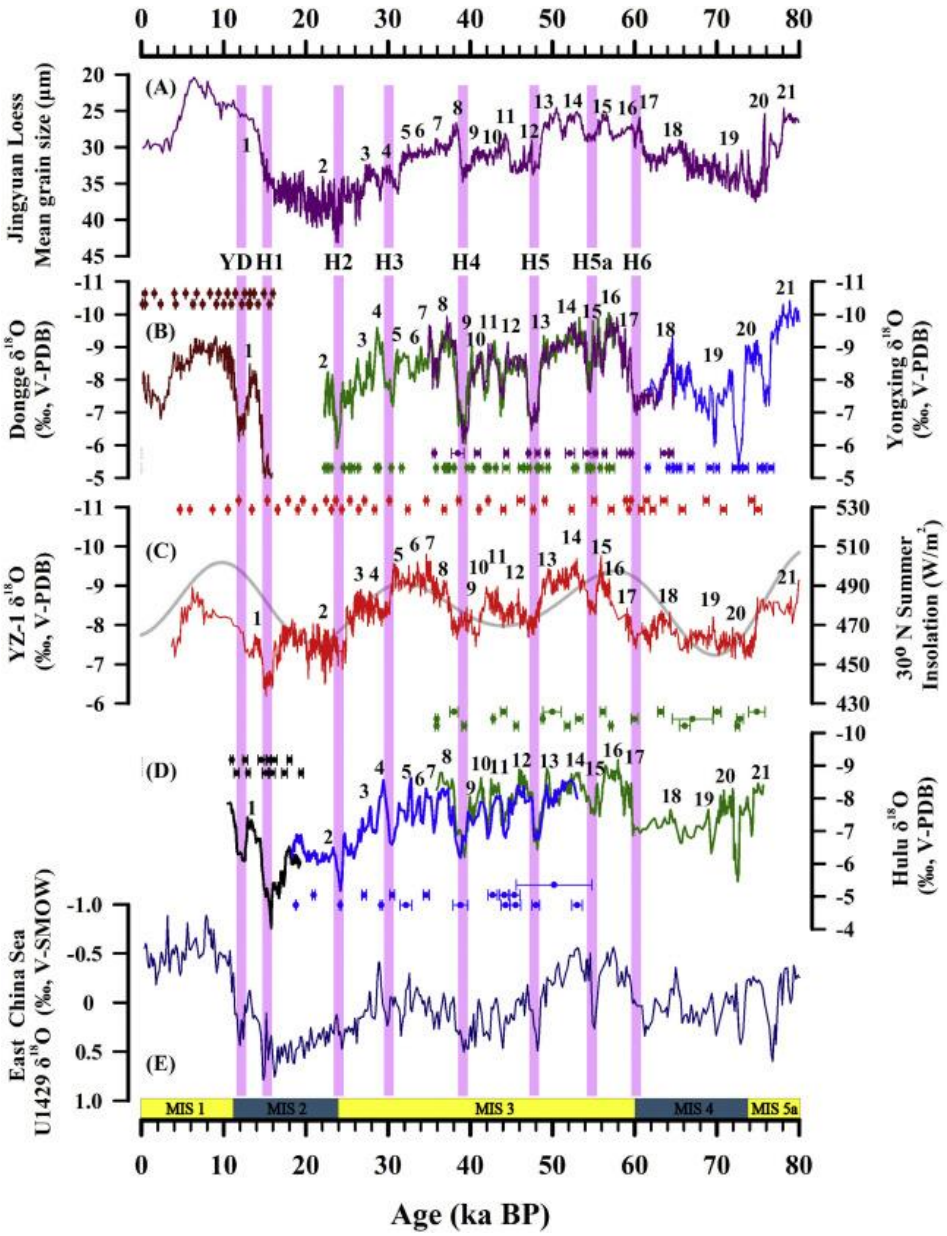

Figure 2. C The last glacial YZ1 d^{18}O record compared with the climatic records in the Asian monsoon region. (A) Jingyuan Loess mean grain size (Sun et al., 2010); (B) Dongge Cave (Yuan et al., 2004) and Yongxing Cave (Chen et al., 2016) stalagmites d^{18}O records (dark red curves indicate Dongge D4 stalagmite, green, purple and blue curves show Yongxing YX51, YX55, and YX46 stalagmite, respectively); (C) The red curve indicates the YZ1 stalagmite d^{18}O record (this study) and the gray curve shows the 30°N summer insolation (Berger and Loutre, 1991); (D) Hulu Cave stalagmites d^{18}O records (Wang et al., 2001) (black, blue and green curves represent PD, MSD, and MLS stalagmite, respectively); (E) International Ocean Discovery Program sediment cores U1429 d^{18}O record (Clemens et al., 2018). The corresponding age control points and age errors of each stalagmite record are expressed bycorresponding colors. The pink vertical bars indicate YD and H events (Heinrich, 1988); the numbers indicate the D-O event (Dansgaard et al., 1993). (For interpretation of the references to color in this figure legend, the reader is referred to the Web version of this article.)

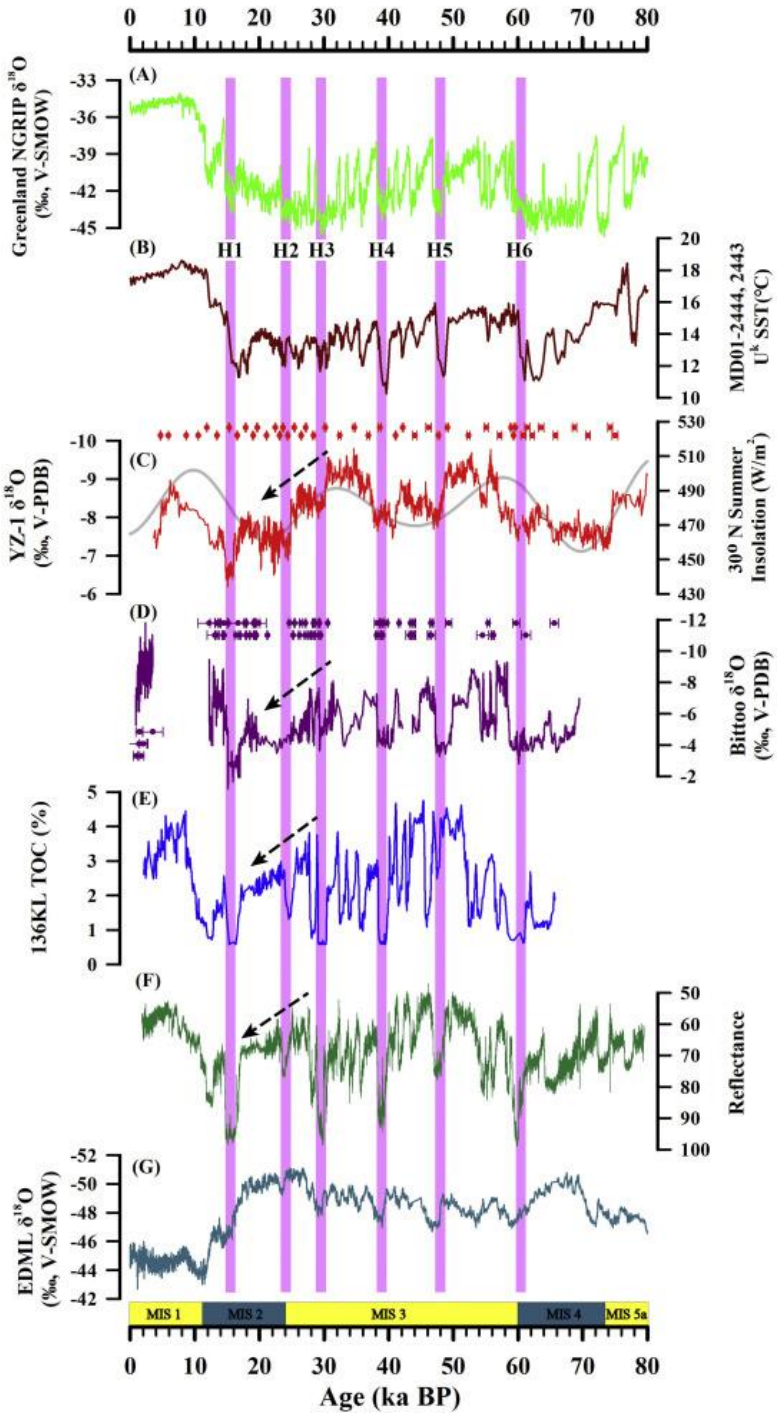

Figure 3. (A) NGRIP ice core d^{18}O record (NGRIP Members, 2004); (B) Sea surface temperature change records reconstructed from the Iberian margin marine sediment cores MD01-2444 and MD01-2443 (Belen et al., 2007); (C) YZ1 stalagmite d^{18}O record (This study). The gray curve shows the 30°N summer insolation (Berger and Loutre, 1991); (D) Bittoo Cave stalagmites d^{18}O records (Kathayat et al., 2016); (E) Arabian Sea sediment cores S90-136 KL TOC record (Schulz et al., 1998); (F) Arabian Sea sediment cores SO130-289 KL reflectance record (Deplazes et al., 2013); (G) Antarctic EDML ice core d^{18}O record (EPICA Community Members, 2006); The pink vertical bars indicate YD and H events (Heinrich, 1988). (For interpretation of the references to color in this figure legend, the reader is referred to the Web version of this article.)

9. 古南海板块构造——来自于地震层析成像的俯冲板块的约束

翻译人：刘伟 inewway@163.com

*Wu J , Suppe J . **Proto-South China Sea Plate Tectonics Using Subducted Slab Constraints from Tomography**[J]. **Journal of Earth Science**, 2018, 29(06):18-32.*

摘要：古南海消失洋盆过去的大小和位置对中生代以来的东南亚板块构造具有重要的意义。在这里，我们展示了利用地震层析成像技术绘制和展开的古南海的古地理新细节。地图上的板块包括:欧亚-南海板块俯冲于马尼拉海沟；北部的菲律宾海板块俯冲于琉球海沟；在南海正下方 450 至 700 公里深处，我们发现了一片孤立的、次水平的板状层析异常，这就是俯冲下去的北部古南海岩石圈。展开的板块显示，在俯冲之前，南海正好位于北部古南海的正上方，两者都在现今马尼拉海沟以东方向展布 400 至 500 公里。我们的板状构造重建表明，古南海被双侧俯冲活动所吞没，主要表现为：(1)北部古南海在渐新世-中新世向南沙和向南扩张的南海俯冲，类似于西地中海盆地的原地自俯冲；(2)古南海有限的南向俯冲于婆罗洲之下发生在渐新世前，也就是 800～900 公里深处的南部古南海板块。

ABSTRACT: The past size and location of the hypothesized proto-South China Sea vanished ocean basin has important plate-tectonic implications for Southeast Asia since the Mesozoic. Here we present new details on proto-South China Sea paleogeography using mapped and unfolded slabs from tomography. Mapped slabs included: the Eurasia-South China Sea slab subducting at the Manila trench; the northern Philippine Sea Plate slab subducting at the Ryukyu trench; and, a swath of detached, subhorizontal, slab-like tomographic anomalies directly under the South China Sea at 450 to 700 km depths that we show is subducted northern proto-South China Sea lithosphere. Slab unfolding revealed that the South China Sea lay directly above the northern Proto-South China Sea with both extending 400 to 500 km to the east of the present Manila trench prior to subduction. Our slab-based plate reconstruction indicated the proto-South China Sea was consumed by double-sided subduction, as follows: (1) The northern proto-South China Sea subducted in the Oligo Miocene under the Dangerous Grounds and southward expanding South China Sea by in-place self subduction similar to the western Mediterranean basins; (2) limited southward subduction of the proto-South China Sea under Borneo occurred pre-Oligocene, represented by the 800 900 km deep southern proto-South China Sea slab.

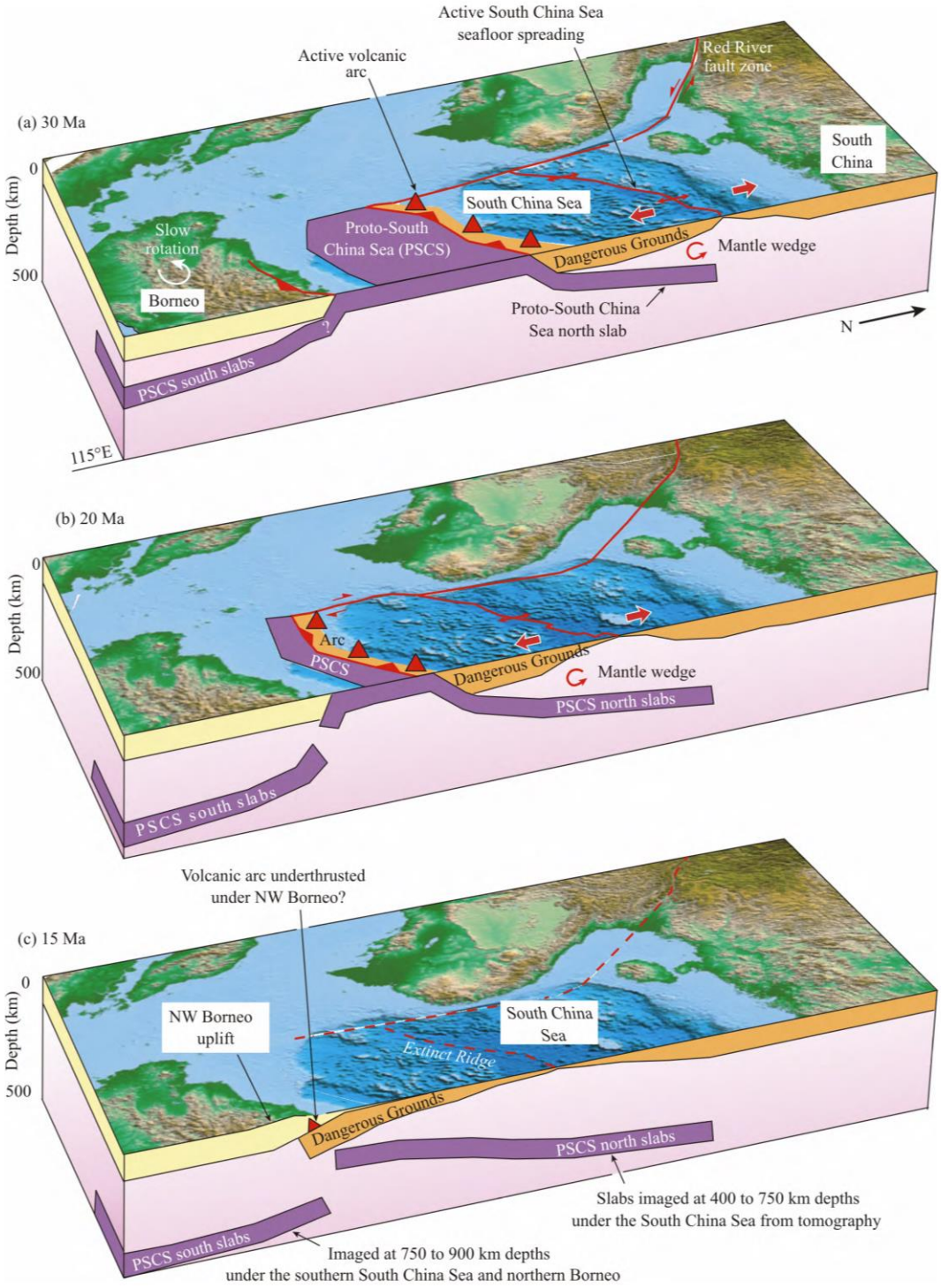

Figure 1. 3D block diagram showing double-sided subduction of the proto-South China Sea between 30 and 15 Ma based on slab constraints (Wu et al., 2016; this study). Opening of the South China Sea after ~34 Ma initiated northward subduction of the 'proto-South China Sea north slabs' beneath the southern Dangerous Grounds. Southward subduction of the 'proto-South China Sea south slabs' under northern Borneo occurred during the Eocene and possibly later due to counter-clockwise Borneo rotations, which are not well time-constrained. Our model implies that during South China Sea seafloor spreading, the southern Dangerous Grounds was an active margin and a mantle wedge formed under the South China Sea. As shown in (c), we suggest the predicted southern Dangerous Grounds volcanic arc was thrust under NW Borneo around ~15 Ma and is no longer at the Earth surface.